

***Development of a multiview time domain
imaging algorithm (MTDI) with a Fermat
correction.***

January 2005

LDRD Engineering Research Final Report 04-ERD-010

Karl Fisher Sean K. Lehman and Dave Chambers

U.S. Department of Energy



Lawrence
Livermore
National
Laboratory

DISCLAIMER

This document was prepared as an account of work sponsored by an agency of the United States Government. Neither the United States Government nor the University of California nor any of their employees, makes any warranty, express or implied, or assumes any legal liability or responsibility for the accuracy, completeness, or usefulness of any information, apparatus, product, or process disclosed, or represents that its use would not infringe privately owned rights. Reference herein to any specific commercial product, process, or service by trade name, trademark, manufacturer, or otherwise, does not necessarily constitute or imply its endorsement, recommendation, or favoring by the United States Government or the University of California. The views and opinions of authors expressed herein do not necessarily state or reflect those of the United States Government or the University of California, and shall not be used for advertising or product endorsement purposes.

This work was performed under the auspices of the U. S. Department of Energy by the University of California, Lawrence Livermore National Laboratory under Contract No. W-7405-Eng-48.

This is an internal report. The opinions and conclusions stated are those of the author and may or may not be those of the Laboratory. This report is not intended to be given external distribution or cited in external documents without the consent of the LLNL Technical Information Department.

This report has been reproduced
directly from the best available copy.

Table of Contents

	Abstract	4
1.0	Introduction	5
2.0	Theoretical Formulation	6
2.1	Derivation of the Forward Model	6
2.2	Generalize the forward model to variable background velocity	10
2.3	Two-dimensional aluminum-copper planar structure	10
3.0	Experimental setup and numerical simulation	11
4.0	Results	13
5.0	Conclusions	13
6.0	Acknowledgements	14
	References	15
	Figures	17

Abstract

An imaging algorithm is presented based on the standard assumption that the total scattered field can be separated into an elastic component with monopole like dependence and an inertial component with a dipole like dependence. The resulting inversion generates two separate image maps corresponding to the monopole and dipole terms of the forward model. The complexity of imaging flaws and defects in layered elastic media is further compounded by the existence of high contrast gradients in either sound speed and/or density from layer to layer. To compensate for these gradients, we have incorporated Fermat's method of least time into our forward model to determine the appropriate delays between individual source-receiver pairs. Preliminary numerical and experimental results are in good agreement with each other.

1 Introduction

Typically, a tomographic reconstruction is derived from a series of *projections*, where a projection is defined as the integral of the image in the direction specified by that angle. Experimentally, this is usually obtained by systematically measuring the transmitted or reflected energies from the object, as it is insonified through a series of angular directions defined by the source-receiver pair [1]. Traditional methods of acoustic/seismic tomography rely on algorithms that can generate a two-dimensional velocity map from a set of line integrals representing the travel time of numerous rays throughout the medium of interest [2,3]. To that end, most straight-ray backprojection algorithms yield single valued reconstructions of either the medium velocity, density, or attenuation, depending on the forward propagation model used and the nature of the probing system [1]. Recently, techniques have been developed to invert acoustic data sets and reconstruct either, density or compressibility maps under specified conditions in tissue [4,5].

The motivation for our development is driven by the need to detect and image flaws in multilayered structures. Application of ultrasonic reflection tomography to non-destructive evaluation of materials is possible, owing to the fact that flaws generally result in weak and localized signals. Thus, the Born approximation can be applied to the scattered field [6]. Our algorithm is based on implementing monopole and dipole expansion terms of a long wavelength scattering result. The implementation we will present generates dual valued reconstructions of the image space, corresponding to the monopole and dipole dependences in the forward model. The approximation of our forward model also admits a single scattering event from a point scatterer, which provides a method for estimating changes in refractive index. The algorithm permits the selection of arbitrary source and receiver locations, thus it can be applied to numerous multistatic data collection geometries and procedures. It can be implemented in either the time or frequency domains but yields better results in the former where all the frequencies are naturally included and do not have to be combined in a synthetic manner after reconstruction.

In most non-destructive evaluation (NDE) problems however, there can be large contrast differences in the acoustic impedances between adjacent layers resulting in significant refraction effects. Various backprojection algorithms have been developed to account for ray bending due to gradients in the background velocity distribution [7]. The significant difference with our application is that a considerable amount of prior knowledge of the internal structure of the part is known: either through blueprints or some other type of manufacturing specification. Thus, for NDE purposes, it is reasonable to assume that the material properties and geometry of the individual layers are well known and understood. In this case, the inverse wave imaging is used to identify deviations, defects, and or flaws in the assembled part.

In the following section, we will present a derivation of our multi-view, time-domain imaging tomography algorithm (MTDI). This is followed by a generalized correction to the forward model for highly refractive media using Fermat's principle of least time [8]. The section ends with an application of the corrected forward model to a representative two-layer aluminum-copper part. A description of the simulation and experiment are given in Section 3. Finally, results for simulated and experimental

reconstructions of the two-layered part are presented in Section 4. Conclusions are discussed in Section 5.

2 Theoretical Formulation

2.1 Derivation of the forward model

From Morse and Ingard [9] equations 8.2.15 and 8.2.19, the *long wavelength* approximation of the scattered field due to a point scatter is

$$\psi^{scat}(\mathbf{R}_m^r, \mathbf{R}_n^t, \mathbf{r}, \omega) = \frac{1}{3} \Phi(\omega) \frac{e^{ikr_m}}{r_m} k^2 a^3 [\gamma_\kappa + \gamma_\rho \cos \theta_{mn}(\mathbf{r})], \quad (1)$$

where

$\psi^{scat}(\mathbf{R}_m^r, \mathbf{R}_n^t, \mathbf{r}, \omega)$	is the measured scattered field at the m -th receiver located at \mathbf{R}_m^r from the n -th source located at \mathbf{R}_n^t ;
\mathbf{r}	is the point scatter location;
$r_m \equiv \mathbf{r} - \mathbf{R}_m^r $	is the distance from the point scatter to the m -th receiver;
ω	is the narrow band frequency;
$k \equiv \omega/c$	is the narrow band wavenumber;
$\Phi(\omega)$	is the spectrum of the incident pulse;
$\gamma_\kappa \equiv \kappa_s - \kappa_o / \kappa_o$	is the relative compressibility ratio;
$\gamma_\rho \equiv 3(\rho_s - \rho_o) / (2\rho_s + \rho_o)$	is the relative density ratio;
θ_{mn}	is the scattering angle;
a	is the point scattering size.

The scattering geometry is presented in Figure 1. The compressibility and density of the scatterer are given as κ_s and ρ_s ; and for the background as, κ_o and ρ_o respectively.

We obtain the time domain representation of the scattered field via,

$$\psi^{scat}(\mathbf{R}_m^r, \mathbf{R}_n^t, \mathbf{r}, t) = \frac{a^3}{3c^2 r_m (2\pi)} [\gamma_\kappa + \gamma_\rho \cos \theta_{mn}(\mathbf{r})] \int_{-\infty}^{\infty} d\omega \omega^2 \Phi(\omega) e^{i\omega r_m/c} e^{-i\omega t}. \quad (2)$$

The inverse Fourier transform yields

$$\begin{aligned} \frac{1}{2\pi} \int_{-\infty}^{\infty} d\omega \omega^2 \Phi(\omega) e^{i\omega r_m/c} e^{-i\omega t} &= \frac{1}{2\pi} \int_{-\infty}^{\infty} d\omega \Phi(\omega) \frac{d^2}{dt^2} e^{-i(t-r_m/c)\omega}, \\ &= \frac{1}{2\pi} \frac{d^2}{dt^2} \int_{-\infty}^{\infty} d\omega \Phi(\omega) e^{-i(t-r_m/c)\omega}, \\ &= \frac{1}{2\pi} \frac{d^2}{dt^2} \phi(t - r_m/c), \end{aligned} \quad (3)$$

resulting in

$$\psi^{scat}(\mathbf{R}_m^r, \mathbf{R}_n^t, \mathbf{r}, t) = \frac{a^3}{6\pi c^2 r_m} [\gamma_\kappa + \gamma_\rho \cos \theta_{mn}(\mathbf{r})] \frac{d^2}{dt^2} \phi(t - r_m/c), \quad (4)$$

as our forward model where $\phi(t)$ is the time-domain pulse.

We consider the arbitrary probing system of Figure 1. A transmitter located at \mathbf{R}_n^t launches an incident field that propagates into the medium. The field interacts with a point scatterer located at \mathbf{r} , and the scattered field is measured at a receiver located at \mathbf{R}_m^r . The scattering angle is θ . In succession, each source transmitter is excited and the scattered field is measured at all of the receivers.¹ Thus, at each receiver, m , we measure the scattered field time series from source, n , to a scatterer located at \mathbf{r} . These time series are represented by $\psi(\mathbf{R}_m^r, \mathbf{R}_n^t, \mathbf{r}, t)$.

In the case where all sources are excited simultaneously, we can view Eq. 4 as representing the *multistatic scattering matrix* and express it as

$$\psi_{mn}(\mathbf{r}) = \frac{1}{r_m} [\hat{\gamma}_\kappa + \hat{\gamma}_\rho \cos \theta_{mn}(\mathbf{r})] \frac{d^2}{dt^2} \phi(t - r_m/c), \quad (5)$$

where the time dependence is implicit but we maintain the spatial dependence to indicate the data are due to a point scatterer at \mathbf{r} , and we have introduced the modified compressibility and density relative ratios, defined as

$$\hat{\gamma}_\rho \equiv \frac{a^3}{6\pi c^2} \gamma_\rho, \quad (6)$$

$$\hat{\gamma}_\kappa \equiv \frac{a^3}{6\pi c^2} \gamma_\kappa. \quad (7)$$

Given a complete set of measurements in the multistatic data matrix, we wish to solve for the modified relative compressibility and relative density ratios. Equation 5 represents a set of $N_c = N_{\text{src}} \times N_{\text{rcv}}$ measurements for the two unknowns where N_{src} is the number of transmitters and N_{rcv} is the number of receivers. In matrix form, Eqn. 5 reads

$$\begin{bmatrix} 1/r_1 & \cos \theta_{1,1}(\mathbf{r})/r_1 \\ 1/r_1 & \cos \theta_{1,2}(\mathbf{r})/r_1 \\ \vdots & \vdots \\ 1/r_1 & \cos \theta_{1,N_t}(\mathbf{r})/r_1 \\ 1/r_2 & \cos \theta_{2,1}(\mathbf{r})/r_2 \\ \vdots & \vdots \\ 1/r_2 & \cos \theta_{2,N_t}(\mathbf{r})/r_2 \\ \vdots & \vdots \\ 1/r_{N_r} & \cos \theta_{N_r,N_t}(\mathbf{r})/r_{N_r} \end{bmatrix} \cdot \begin{bmatrix} \hat{\gamma}_\kappa \\ \hat{\gamma}_\rho \end{bmatrix} = \begin{bmatrix} \psi_{1,1}(\mathbf{r}) \\ \psi_{1,2}(\mathbf{r}) \\ \vdots \\ \psi_{1,N_t}(\mathbf{r}) \\ \psi_{2,1}(\mathbf{r}) \\ \vdots \\ \psi_{2,N_t}(\mathbf{r}) \\ \vdots \\ \psi_{N_r,N_t}(\mathbf{r}) \end{bmatrix}, \quad (8)$$

where the scattering angle is given by

¹ Technically, the *total* field is measured. The *scattered* field is obtained from the difference between the *total* field and the *incident* field.

$$\cos\theta_{mn}(\mathbf{r}) \equiv -\frac{(\mathbf{r} - \mathbf{R}_m^r) \cdot (\mathbf{R}_n^t - \mathbf{r})}{|\mathbf{r} - \mathbf{R}_m^r| |\mathbf{R}_n^t - \mathbf{r}|}. \quad (9)$$

Eqn. 8 is of the form

$$A\mathbf{g} = \mathbf{k}, \quad (10)$$

where A , is a $N_c \times 2$ matrix of $1/r_m$ and cosine terms of the scattering angle, \mathbf{g} is the 2×1 vector of unknown modified relative compressibility and relative density ratios, and \mathbf{k} is the $N_c \times 1$ vector of values from the multistatic data matrix.

The $\psi_{mn}(\mathbf{r})$ values are obtained in one of two different methods. The first method, the *time domain method*, is to compute the total travel time, using the background velocity, from the source to the scatterer, and then from the scatterer to the receiver, and select the time series value at that time. One can optionally add to this travel time a delay to the pulse maximum. For example, if $\phi(t)$ is the transmitted pulse, and T_d is the time to the pulse maximum defined as

$$T_d \equiv \arg \max_t |\phi(t)|, \quad (11)$$

then $\psi_{mn}(\mathbf{r})$ is the value of the received time series evaluated at

$$t_{mn}(\mathbf{r}) \equiv |\mathbf{R}_n^t - \mathbf{r}|s_o + |\mathbf{r} - \mathbf{R}_m^r|s_o + T_d \quad (12)$$

where s_o , is the slowness of the background medium defined as $s_o = 1/v_o$, where v_o is the bulk velocity of the background media. The second method is a *frequency domain method* in which the Fourier transform of the multistatic data matrix series is computed, and $\psi_{mn}(\mathbf{r})$ is set equal to the value of the Fourier series peak at the frequency multiplied by a phase delay given by $e^{\pm i t_{mn}(\mathbf{r}) \omega}$ where the \pm depends upon the sign of the forward Fourier transform.

In this development, we have chosen the *time domain* method, Eqn. 10 is solved by

$$\mathbf{g} = \left(A^\dagger A \right)^{-1} A^\dagger \mathbf{k}.$$

Explicitly, we have,

$$A^\dagger A = \begin{bmatrix} N_t \sum_{mn} \frac{1}{r_m^2} & \sum_{mn} \frac{\cos\theta_{mn}(\mathbf{r})}{r_m^2} \\ \sum_{mn} \frac{\cos\theta_{mn}(\mathbf{r})}{r_m^2} & \sum_{mn} \left(\frac{\cos\theta_{mn}(\mathbf{r})}{r_m} \right)^2 \end{bmatrix}, \quad (13)$$

$$A^\dagger \mathbf{k} = \begin{bmatrix} \sum_{mn} \frac{\psi_{mn}(\mathbf{r})}{r_m} \\ \sum_{mn} \frac{\cos \theta_{mn}(\mathbf{r}) \psi_{mn}(\mathbf{r})}{r_m} \end{bmatrix}. \quad (14)$$

Thus

$$(A^\dagger A)^{-1} = \frac{1}{\Delta} \begin{bmatrix} \sum_{mn} \left(\frac{\cos \theta_{mn}(\mathbf{r})}{r_m} \right)^2 & -\sum_{mn} \frac{\cos \theta_{mn}(\mathbf{r})}{r_m^2} \\ -\sum_{mn} \frac{\cos \theta_{mn}(\mathbf{r})}{r_m^2} & N_t \sum_{mn} \frac{1}{r_m^2} \end{bmatrix}, \quad (15)$$

where the determinant is

$$\Delta \equiv \left(N_t \sum_{mn} \frac{1}{r_m^2} \right) \sum_{mn} \left(\frac{\cos \theta_{mn}(\mathbf{r})}{r_m} \right)^2 - \left(\sum_{mn} \frac{\cos \theta_{mn}(\mathbf{r})}{r_m^2} \right)^2. \quad (16)$$

Solving for \mathbf{g} , we find,

$$\begin{bmatrix} \hat{\gamma}_\kappa \\ \hat{\gamma}_\rho \end{bmatrix} = \frac{1}{\Delta} \begin{bmatrix} \sum_{mn} \left(\frac{\cos \theta_{mn}(\mathbf{r})}{r_m} \right)^2 & -\sum_{mn} \frac{\cos \theta_{mn}(\mathbf{r})}{r_m^2} \\ -\sum_{mn} \frac{\cos \theta_{mn}(\mathbf{r})}{r_m^2} & N_t \sum_{mn} \frac{1}{r_m^2} \end{bmatrix} \begin{bmatrix} \sum_{mn} \frac{\psi_{mn}(\mathbf{r})}{r_m} \\ \sum_{mn} \frac{\cos \theta_{mn}(\mathbf{r}) \psi_{mn}(\mathbf{r})}{r_m} \end{bmatrix}, \quad (17)$$

$$= \frac{1}{\Delta} \begin{bmatrix} \sum_{mn} \left(\frac{\cos \theta_{mn}(\mathbf{r})}{r_m} \right)^2 \left(\sum_{mn} \frac{\psi_{mn}(\mathbf{r})}{r_m} \right) - \left(\sum_{mn} \frac{\cos \theta_{mn}(\mathbf{r})}{r_m^2} \right) \left(\sum_{mn} \frac{\cos \theta_{mn}(\mathbf{r}) \psi_{mn}(\mathbf{r})}{r_m} \right) \\ \left(N_t \sum_{mn} \frac{1}{r_m^2} \right) \left(\sum_{mn} \frac{\cos \theta_{mn}(\mathbf{r}) \psi_{mn}(\mathbf{r})}{r_m} \right) - \left(\sum_{mn} \frac{\cos \theta_{mn}(\mathbf{r})}{r_m^2} \right) \left(\sum_{mn} \frac{\psi_{mn}(\mathbf{r})}{r_m} \right) \end{bmatrix}. \quad (18)$$

Finally,

$$\kappa_s = (1 + \hat{\gamma}_\kappa) \kappa_o, \quad (19)$$

and

$$\rho_s = \frac{3 + \hat{\gamma}_\rho}{(2\hat{\gamma}_\rho - 3)} \rho_o. \quad (20)$$

2.2 Generalize the forward model to a variable background velocity

The analysis thus far has assumed a constant slowness $s(\mathbf{r}) = s_o$ throughout the imaged region. Implicit in this assumption is that the incident and scattered acoustic fields propagate following straight ray paths from transmitter location \mathbf{R}_n^t to the scatterer at \mathbf{r} and from the scatterer to the receiver location \mathbf{R}_m^r . Depending upon the severity of the spatial velocity gradients, this assumption is often a very poor approximation. In this section, we will present a correction to the forward model given in Eqn. 4 that utilizes Fermat's principle of least time.

Fermat's principle of least time selects the ray that minimizes the travel time between a specified transmitter location, \mathbf{R}_n^t to a receiver located at \mathbf{R}_m^r . Let us consider an arbitrary path P denoted in this case by the vectors $(\mathbf{R}_n^t - \mathbf{r})$ and $(\mathbf{r} - \mathbf{R}_m^r)$ that connects a given source-receiver pair in Figure 1. The travel time for this particular source receiver pair is denoted as

$$\tau^P(s) = \int_P s(\mathbf{x}) dl^P, \quad (21)$$

with \mathbf{x} describing the vector connecting the source-receiver pair through the scatterer at \mathbf{r} and dl^P corresponding to an infinitesimal distance along path P . Fermat's principle states that the *correct* ray path is one that connects the source receiver pair with the minimum travel time. Stated another way, Fermat's principle stipulates that the travel time integral is *stationary* with respect to variations in the ray path [10]. Thus, from Figure 1 the travel time between a given source-receiver pair is

$$t_{m,n}^f = \min_{P_1 \in Paths} \left\{ \int_{P_1} s(x) dl^{P_1} \right\} + \min_{P_2 \in Paths} \left\{ \int_{P_2} s(x) dl^{P_2} \right\}, \quad (22)$$

where P_1 is the path from transmitter \mathbf{R}_n^t to scattering location \mathbf{r} , P_2 is the path from the scattering location to the receiver \mathbf{R}_m^r . The notation, $P_i \in paths$, means that P is a member of the set of possible paths connecting the source receiver pair. We will now apply this generalized formulation to a two-dimensional planar problem.

2.3 Two-dimensional aluminum-copper planar structure

Consider the planar multilayer geometry shown in Figure 2. We assume that the aperture of the imaging array is located along the upper surface of layer 1, and that at each sensor location the transducer can act as either a transmitter or as a receiver of acoustic energy. As before, n , is the index number for a defined set of transmitters ($n = 1, N_{src}$) and m , is the index number for a defined set of receivers ($m = 1, N_{rcv}$). The planar geometry gives rise to the following set of functional equations. The first relates the time of flight from a transmitter location $[\mathbf{R}_{x,n}^t, \mathbf{R}_{y,n}^t]$ to a scatterer at location (x_i, y_i)

$$t_n^f(x_i, y_i) = \min_{\eta \in Paths} \left\{ \frac{\left((\eta - R_{x,n}^t)^2 + (l_{Al} - R_{y,n}^t)^2 \right)^{\frac{1}{2}}}{c_{Al}} + \frac{\left((x_i - \eta)^2 + (y_i - l_{Al})^2 \right)^{\frac{1}{2}}}{c_{Cu}} \right\}, \quad (23)$$

and the second relates the time of flight from the scatterer at, (x_i, y_i) , to a receiver at location, $[R_{x,m}^r, R_{y,m}^r]$

$$t_m^f(x_i, y_i) = \min_{\sigma \in Paths} \left\{ \frac{\left((x_i - \sigma)^2 + (y_i - l_{Al})^2 \right)^{\frac{1}{2}}}{c_{Cu}} + \frac{\left((l_{Al} - R_{y,m}^r)^2 + (R_{x,m}^r - \sigma)^2 \right)^{\frac{1}{2}}}{c_{Al}} \right\}. \quad (24)$$

Here the notation, $\eta \in paths$ refers to the set of all possible ray intersections from a transmitter location $[R_{x,n}^t, R_{y,n}^t]$, through the interface at l_{Al} to the location (x_i, y_i) . Similarly, $\sigma \in paths$ refers to the set of all possible ray intersections from the location (x_i, y_i) , through the interface at l_{Al} to a receiver located at $[R_{x,m}^r, R_{y,m}^r]$. The minimum total time between the source to the scattering location and then to the receiver is simply

$$t_{mn}^f(x_i, y_i) = t_n^f(x_i, y_i) + t_m^f(x_i, y_i) + T_d. \quad (25)$$

Equation 25 defines the variable velocity *minimum* travel time for our planar geometry, where the similarities to Eq 12 are apparent.

3 Experimental setup and numerical simulation

The experimental data were collected using a computer controlled 32-channel pulser-receiver data acquisition system connected to a single 32-element 5MHz ultrasonic array [11]. The system has the capability of transmitting arbitrary waveforms and receiving on all channels. The array was mounted on the upper surface of two-layer aluminum-copper test part. The aluminum layer was 13mm thick; the copper layer was 9 mm thick. A “defect” in the form a 1 mm hole was drilled into the copper layer such that the axis of the hole was parallel with the planar layer interfaces. A schematic of the test part and the array are shown in Figure 3. Data sets were recorded in a full multistatic process whereby each source sequentially ensonified the medium with a broadband pulse centered at 5 MHz and the corresponding scattered field was recorded on all of the receivers. Following this procedure, one would obtain a three dimensional data set comprising the sampled time record for all possible source and receiver locations. Mathematically this corresponds to data matrix A of the form $N_{src} \times N_{rcv} \times N_t$ where N_t is the number of samples in the voltage timeform, N_{src} are the number of transmitters and, N_{rcv} , is the number of receivers.

In addition to the experiment, a two-dimensional numerical simulation was performed to generate additional data sets for comparison. The simulation results were

obtained using E3D, an explicit finite-difference time domain code developed at Lawrence Livermore National Laboratory [12-17]. The code can simulate full wave scattering phenomena in elastic or coupled fluid-elastic systems in either two or three dimensions. The required input parameters are a longitudinal velocity distribution, a transverse velocity distribution, and a density distribution. The model is comprised of four layers: air, aluminum, copper and air. The “defect” is an air filled circular region 1mm in diameter in the copper layer. The numerical region and the material properties are listed in Figure 2.

Simulations and the experiments used the same Gaussian windowed pulse shape:

$$u(t) = \sin(\omega_o t) e^{-t^2/(2\sigma^2)} \quad (26)$$

where $\omega_o \equiv 2\pi f_o$, $\sigma \equiv N_{cyc}/\omega_o$ and N_{cyc} is the number of cycles in the pulse. We used $f_o = 5$ MHz and $N_{cyc} = 5$ cycles. For the experiment, this pulse is actually defined in terms of voltage. However, in the simulation, it is defined as a normal stress applied at a source location. A spectral comparison conducted on an experimental pulse measured in a simple pulse-echo geometry, and the corresponding simulated pressure pulse reveal only slight differences in their respective frequency content. We can assert, that the voltage-to-pressure transfer function is constant over the bandwidth of the applied pulse. Thus, normalized images created using numerical data and experimental data can be compared directly. All the experimental measurements were taken using a 32 channel RDTech TRM system [11]. This custom hardware-software system allows for the individual control of each transducer element with arbitrary transmit pulse capabilities. The transmit-receive array was designed to operate at 5MHz with an element to element pitch of approximately 1mm. The element height is 10mm. Voltage-time records for each receive element can easily be recorded and stored as RF waveforms on the host PC. Reconstruction algorithms were conducted on a separate computer.

The reconstruction process requires a multistatic data set representing the *scattered* field in the elastic region of interest. Multistatic data refers to the process in which one element of the array acts a transmitter to ensonify the test region. The return time-series signals (echoes) are subsequently recorded on *all* of the elements; this process is repeated at all of the transmit-receive locations. To that end, we began by recording a *background* data set. See Figure 3. The *background* data can be obtained from an identical part, or a region on the same part, that is free of defects². For our purposes, the *background* data were obtained by locating the transducer array over a region of the aluminum-copper plate far enough away from the hole to eliminate any reflections. A complete multistatic background data set was recorded. The array was then moved to a region over the flaw, as shown in Figure 3, and a second complete multistatic data set was recorded. This data set is referred to as the *object* data set. The complete multistatic *scattered* data set is then the difference between the *object* data set and the *background* data set. In a similar manner, numerical simulations of the multistatic data were generated for the *background* (no flaw) and *object* (flaw present) data sets.

² Recall, that because we are applying this algorithm as a non-destructive imaging technique we have access to *a priori* knowledge of the system without defects either through initial inspections or mechanical specifications.

4 Results

The resulting reconstructions using simulated and experimental data are shown in Figures 4 and 5 respectively. The upper figure represents a map of the *modified* relative compressibility ratio, while the lower figure represents a map of the *modified* relative density ratio, (see Eq. 6 and 7) for the imaged region. The actual location of the aluminum-copper interface and the flaw are included for reference. The lambda metric is the wavelength in the aluminum layer at $f_0 = 5$ MHz.

The reconstruction of the simulated data clearly shows the flaw correctly located in the copper layer. The moderate haloing effect around the hole is a result of diffraction and shear wave effects in the immediate region surrounding the hole. The artifacts to the far left of the hole are a result of multiple reflections in the *scattered* field occurring in the aluminum and copper layers. Even with the subtraction process, which effectively removes the incident field and its multiples, the scattered field will become more complex with time reducing the quality of the reconstruction. The present algorithm does not take into account multi-path scattering effects. However, if we limit the length of the time records used for the reconstruction to approximately the time of flight of a return arrival from the lower copper boundary, then these types of errors can be mitigated.

Reconstructions of the experimental data show a visible flaw, correctly located in the lower copper layer. A strong indication of the interface between the aluminum and copper layers is also present. In this case the subtraction process did not remove the incident field completely. This could result from slight changes between the background data set and the object data set due to location and bond differences. Note, that this type of effect could be included into the simulated data. In the actual part, the bond line between the aluminum and the copper has a finite thickness of approximately 0.003" (0.076mm) and with significantly different acoustic impedance ($Z_{\text{epoxy}} = 3.2$ mks Rayles, verses $Z_{\text{Al}} = 17$ mks Rayles and $Z_{\text{Cu}} = 42$ mks Rayles). A finite bond thickness is not accounted for in the reconstruction model. The experimental image contains more artifacts than the simulated image, owing to the systematic problems associated with subtracting the background data from the object data, random noise in the recorded data and part variability. Even with these issues, the images clearly show accurate localization and acceptable contrast of the flaw within the part geometry.

6 Conclusions

An algorithm has been developed for imaging and characterization of elastic structures that have high contrast gradients in either compressibility (velocity) and or density. Applying the standard monopole and dipole expansion terms of a long wavelength acoustic scattering approximation, in conjunction with a concise matrix approach, we have obtained separate image maps corresponding to these monopole and dipole terms. A bent ray correction method utilizing Fermat's method of least time is incorporated into the forward model to accommodate ray-bending effects in the layered system. Future work will be directed towards developing a quantitative version of this algorithm where

by the inversion generates reconstructions that are directly proportional to the mediums density and compressibility.

7 Acknowledgements

We wish to thank Jim Candy for use of his data acquisition system. This work was performed under the auspices of the U. S. Department of Energy by the University of California, Lawrence Livermore National Laboratory under contract W-7405-48.

References

- [1] A. C. Kak and M. Slaney. *Principles of Computerized Tomographic Imaging* IEEE Press, 1988. ISBN 0-7803-0447-0.
- [2] J. G. Berryman, Stable iterative reconstruction algorithm for nonlinear traveltime tomography. *Inverse Problems*, **6** (21-42), 1990.
- [3] S. A. Enright, S. M. Dale, V. A. Smith, R. D. Murch and R. T. Bates, Towards solving the bent-ray tomographic problem. *Inverse Problems*, **8**, (83-94), 1992.
- [4] S. J., Norton, Generation of separate density and compressibility images in tissue, *Ultrason. Imaging*. vol. 5, pp. 240-252.
- [5] S. Mensah, J.,P., Lefebvre, Enhanced compressibility tomography, *IEEE Trans. Ultrason. Ferro. and Freq. Cntrl. Vol. 44 no. 6.* ,Nov 1997, pp 1245-1252.
- [6] J.,P., Lefebvre, P. Recotillet, P. Lasaygues, NDE application of ultrasonic reflection tomography, 1994 *IEEE Ultrason. Symp. Proc.* IEEE Press, New York, pp 11289-1292.
- [7] M. Kueger, V. Burow, K. M. Hiltawsky, H. Everet, Limited angle ultrasonic tomography of the compressed female breast, 1998 *IEEE Ultrason. Symp. Proc.* IEEE Press, New York, pp 1345-1348.
- [8] J.A. Scales. *Theory of Seismic Imaging*, Samizdat Press, 1994.
- [9] P.M. Morse and K.U. Ingard. *Theoretical Acoustics*, Princeton University Press, 1968. ISBN 0-691-02401-4.
- [10] M. Born and E. Wolf, *Principles of Optics* (Pergamon, London, 1959) 127-129.
- [11] R/D Tech, TomoScan System, 4495, Wilfrid-Hamel Blvd., Québec (Québec), G1P2J7, Canada
- [12] A. R. Levendar, Forth-order finite-difference p-sv seismograms. *Geophysics*, **53**:1425-1436, 1988.
- [13] S. Larsen and J. Greiger. Elastic modeling initiative, part III: 3-D computational modeling. *Soc. Expl. Geophys. Confer. Proc.* **68**:1803-1806, 1998.

- [14] S. Larsen, M. Antolik, and *et al.* 3D simulations of scenario earthquakes in the San Francisco Bay Area, *EOS Trans.*, **78**:487, 1997.
- [15] R. Madariaga. Dynamics of an expanding circular fault. *Bulletin of the Seismological Society of America*, **66**(3):639-666, June 1976.
- [16] J. Viriux. P-SV wave propagation in heterogeneous media, Velocity-stress finite-difference method. *Geophysics* **51**(4):889-901, April 1986.
- [17] Shawn Larsen and David Harris, Seismic wave propagation through a low-velocity nuclear rubble zone. Technical Report, Lawrence Livermore National Laboratory, 7000 E. Avenue, Livermore. CA, 94550, 1993.

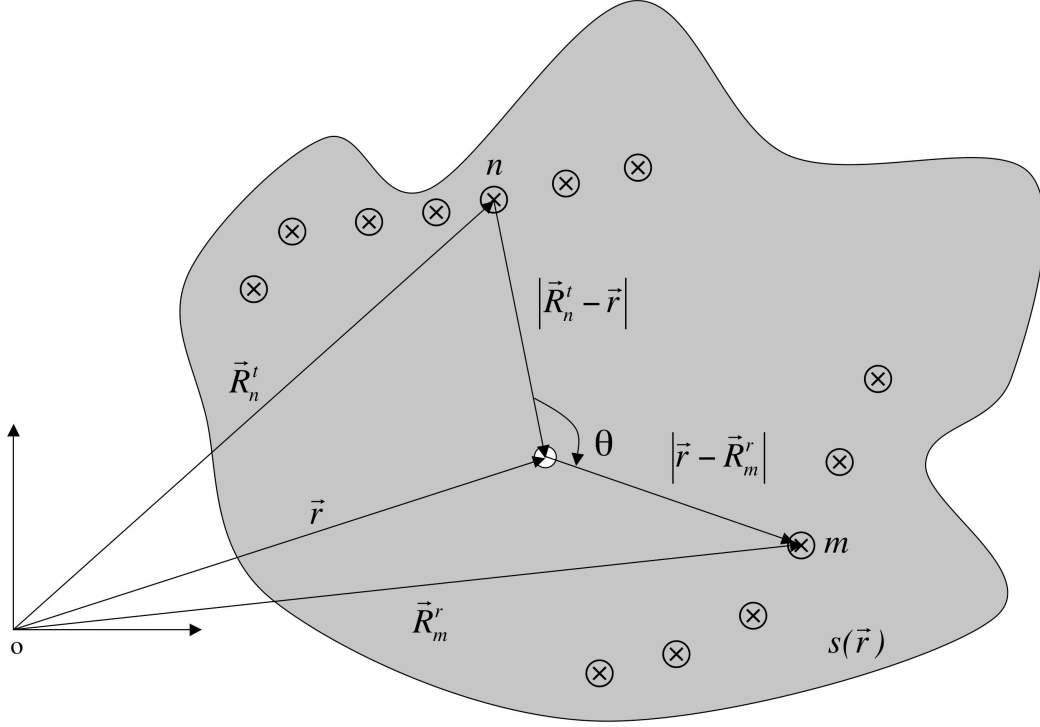


Figure 1. Arbitrary wave probing system where the sensor locations are denoted as \otimes . The slowness distribution for the medium is given by $s(\mathbf{r}) = 1/v(\mathbf{r})$, where $v(\mathbf{r})$ is the corresponding bulk velocity distribution of the background medium.

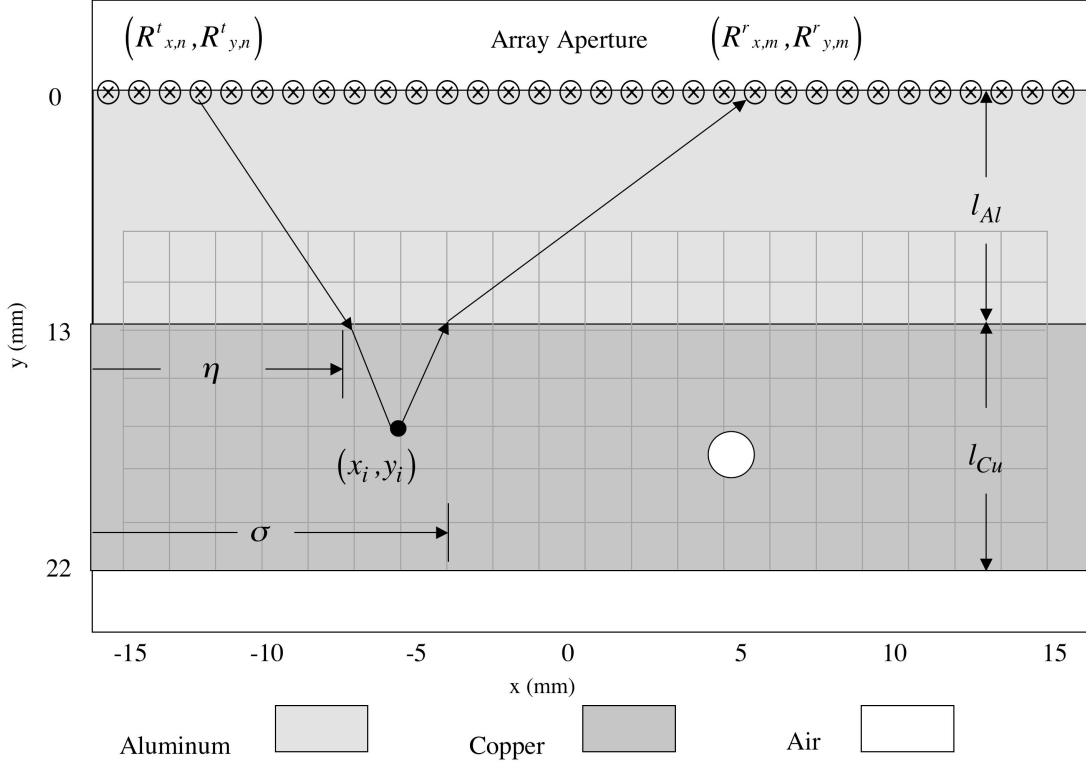


Figure 2. The planar multilayered system. The grid locations correspond to the image reconstruction region. The finite difference time domain grid is much finer and not shown. The longitudinal sound speed and density of the system are defined where, $c_{Al} = 6.32\text{mm/us}$ and $\rho_{Al} = 2.7\text{g/cm}^3$ are the longitudinal sound speed and density of aluminum respectively; and $c_{Cu} = 4.66\text{ mm/us}$, $\rho_{Cu} = 8.98\text{ g/cm}^3$, are the longitudinal sound speed and density of copper. The longitudinal sound speed and density of air is $c_{air} = 0.344\text{ mm/us}$, $\rho_{air} = 0.012\text{ gm/cm}^3$.

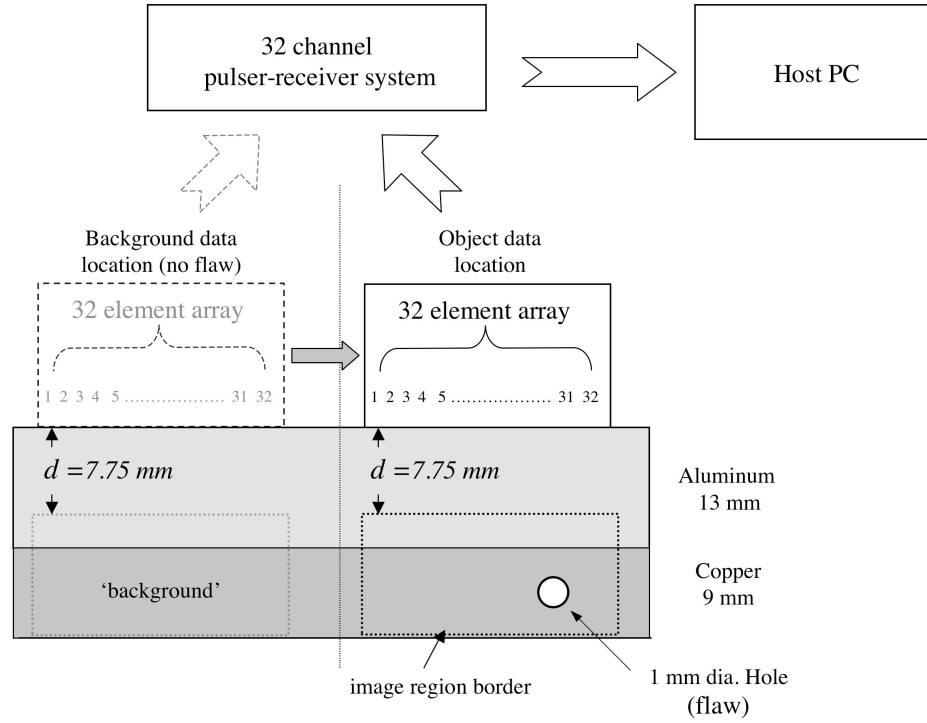


Figure 3. Experimental setup and multi-channel data acquisition hardware [11]. Two separate multistatic data sets are obtained, a *background* scan and then an *object* scan. The background scan location is chosen in a region free of flaws. The object scan location is chosen such that the flaw is insonified by the imaging array.

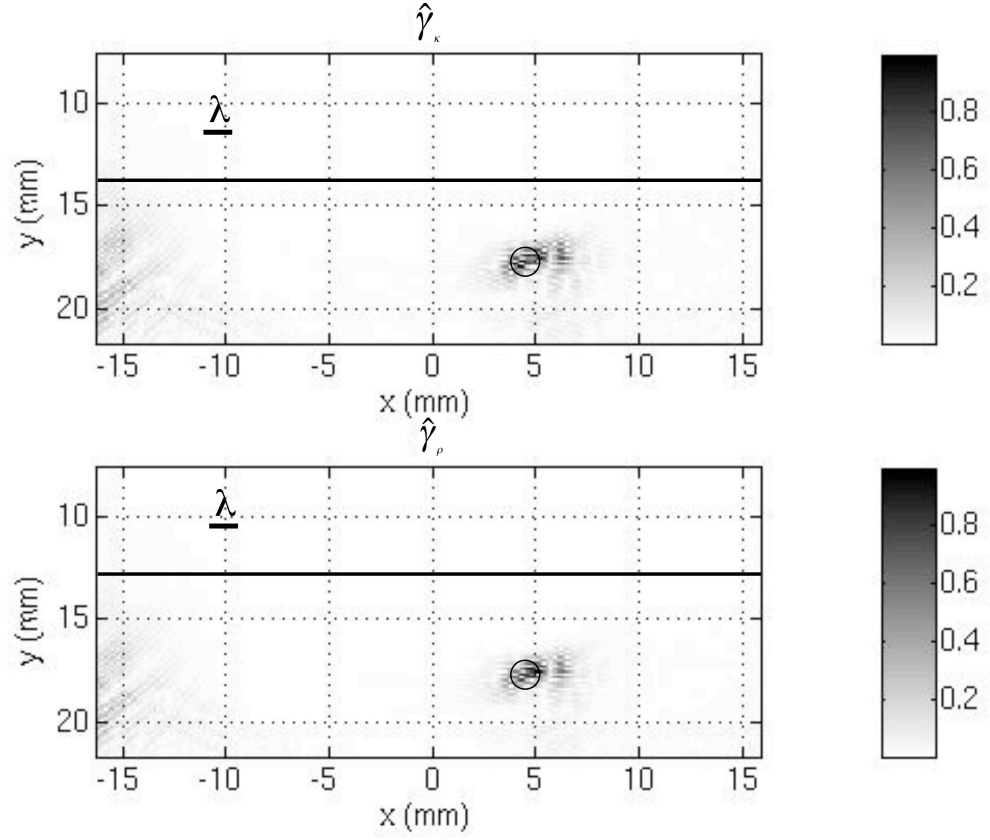


Figure. 4 Reconstructions of *simulated* data using the MTDI algorithm. Limited view aperture. The aluminum-copper interface and location of the hole are superimposed on the image for reference. The images clearly show the flaw correctly located in the copper layer. The λ metric is the wavelength of the field in the top aluminum layer at $f_o = 5\text{MHz}$.

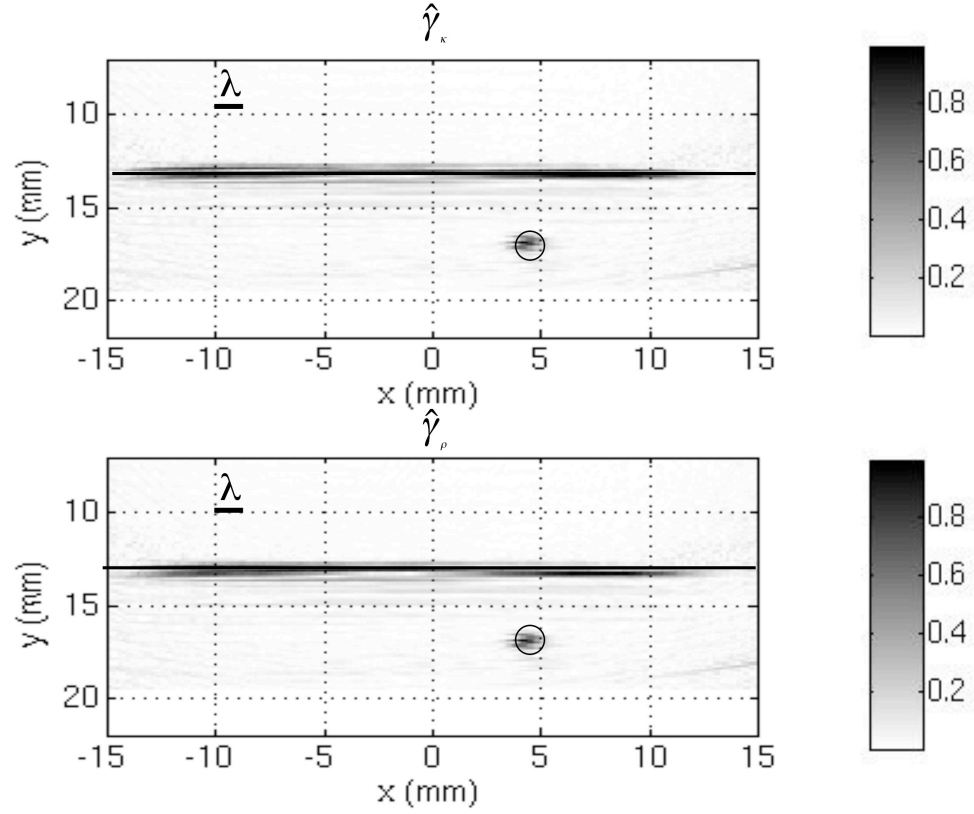


Figure 5: Reconstructions of *experimental* data using the MTDI algorithm. Limited view aperture. The aluminum-copper interface and location of the hole are superimposed on the image. A strong indication of the interface between the aluminum and copper layers is also present. In this case the subtraction process did not remove the incident field completely. This could result from slight changes between the background data set and the object data set due to location and bond differences. The λ metric is the wavelength of the field in the top aluminum layer at $f_0 = 5\text{MHz}$.